OPEN ACCESS
IOP Publishing | International Atomic Energy Agency
Nuclear Fusion
Nucl. Fusion **63** (2023) 096017 (10pp)
https://doi.org/10.1088/1741-4326/ace3d9

Time-dependent collisional radiative modeling of tungsten in the magnetic sheath for erosion diagnosis

C.A. Johnson[1,2,*], D.A. Ennis[1], S.D. Loch[1] and C.P. Ballance[3]

[1] Auburn University, Auburn, AL, United States of America
[2] Oak Ridge Institute for Science and Education (ORISE), Oak Ridge, TN, United States of America
[3] Queens University Belfast, Belfast BT7 1NN, United Kingdom of Great Britain and Northern Ireland

E-mail: johnsonca@ornl.gov

Received 7 March 2023, revised 12 June 2023
Accepted for publication 4 July 2023
Published 9 August 2023

Abstract

Tungsten is the material of choice for the divertors in ITER, SPARC and future fusion reactors. Accurate diagnosis of tungsten erosion and migration is important for first wall life time, slag production and core performance. The addition of a magnetic presheath requires time-dependent collisional radiative effects to be included for accurate neutral tungsten collisional radiative modeling. Gross erosion measurements could be modified by a factor of 10 due to the inclusion of time-dependent effects for ITER relevant divertor conditions. A simple sputtering model and sheath density model are developed to investigate time-dependent collisional radiative effects. Neutral tungsten spectral lines populated from different metastable levels depend on model parameters leading to potential spectroscopic diagnostics of plasma parameters. Electron temperatures inferred from spectroscopic line ratios are in agreement with Langmuir probe measurements in the Compact Toroidal Hybrid.

Keywords: tungsten, S/XB, ColRadPy, collisional radiative, metastable state, erosion

(Some figures may appear in colour only in the online journal)

1. Introduction

Understanding plasma-material interaction continues to be a challenge for future fusion reactors. High-Z materials (e.g. tungsten, molybdenum) are an anticipated solution for plasma facing materials as they satisfy requirements for power exhaust, thermal conductivity and melting point while minimizing tritium retention. Current models predict that wall erosion could be on the order of thousands of kilograms per year [1]. Thus, there is a need to understand these models, as a concentration of W as low as 10^{-5} is predicted to degrade core plasma performance [2]. Many domestic and international fusion relevant devices have upgraded or have plans to upgrade to high-Z PFCs. DIII-D has previously installed W PFCs [3] and recently install the tungsten Small Angle Slot divertor [4]. JET has upgraded to the W/Be ITER-like wall, and both ASDEX-U and WEST have a majority of PFCs made from W. Tracking the transport of tungsten from the wall to the core has also been the focus of previous investigations [5–8]. Nonetheless, edge impurity transport models such as DIVIMP and ERO 2.0 have difficulty matching experimental measured erosion rates [9, 10]. The resolution of this disagreement would be instrumental in obtaining better predictive models of W leakage.

A significant international effort has been underway to better quantify the erosion of high-Z materials. Next step fusion experiments might have orders of magnitude more

* Author to whom any correspondence should be addressed.

erosion and subsequent redeposition than present fusion relevant devices. Preparation for these machines will require extrapolation from current models of high-Z erosion and leakage. As such, machine design parameters could be significantly impacted by the accuracy of these models used for extrapolation.

A new time-dependent sheath model for Collision Radiative (CR) modeling of tungsten has been developed to provide Generalized Radiative Coefficients (GCRs) for gross erosion measurements. The sensitivity of the model to parameters with large associated uncertainties, such as the initial atomic metastable fraction of sputtered tungsten and the sputtering velocity, is investigated by varying these parameters to determine their impact on the CR model. A detailed description of both the collisional radiative model and sheath model are provided in section 2. The setup and operation of a new high-resolution ultraviolet spectrometer installed on the Compact Toroidal Hybrid (CTH) torsatron for comparisons with collisional radiative modeling predictions is detailed in section 2.3. Results from the time-dependent sheath model are presented in section 3 including an investigation of sensitivity to the model parameters. Finally, a comparison of CTH experimental data and the time-dependent sheath model is shown in section 4.

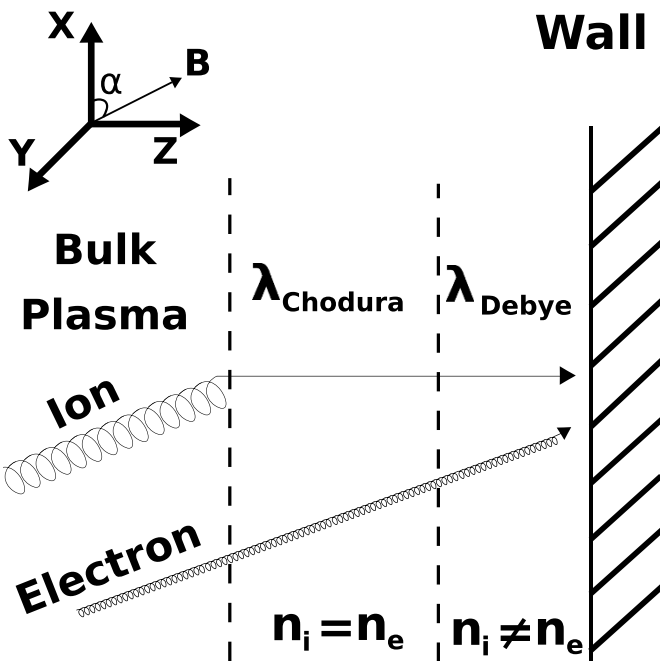

Figure 1. Diagram of the plasma sheath consisting of the bulk plasma (left), the CS (middle) and the DS (right) separated by the dashed lines. Note that the illustration is not to scale; the CS is much wider than the DS.

2. Methods

2.1. Neutral tungsten atomic data and collisional radiative model

Both spectral emission modeling and erosion measurements performed with the S/XB method require atomic transition rates such as electron-impact excitation/de-excitation and ionization to be calculated [11]. The accuracy of any emission or erosion diagnostic is directly related to the accuracy of the atomic data employed. The basic atomic data used for the CR model in this work is derived from Johnson *et al* [12], with the electron-impact excitation rates coming from a new, non-perturbative Dirac R-matrix electron-impact calculation performed by Smyth *et al* [13] and ionization is evaluated using the Exchange Classical Impact Parameter method [14]. Collisional Radiative modeling was completed using the open-source ColRadPy CR suite of codes [15].

2.2. Sheath model

The large heat flux onto plasma facing components (particularly in the divertor) in a fusion reactor will require oblique incident angles of particles on surfaces. Smaller angles effectively reduce the heat flux to PFCs allowing for reactors to operate at higher power densities. The Chodura Sheath (CS) [16] arises from the gyro-motion effects of ions and electrons at oblique angles. Unlike the Debye Sheath (DS), the CS, also known as the Magnetic Presheath (MPS), is quasi-neutral; however, there is a significant electric field oriented perpendicular to the surface. The CS is also significantly thicker than the DS (on the order ion Larmor radius compared to the Deybe length). A diagram of the plasma sheath region with the addition of the CS is depicted in figure 1. The model developed by Chodura is constrained by boundary conditions on both sides of the CS. The Chodura criterion requires that the ion velocity be equal to or greater than the sound speed at the angle of the magnetic field. The boundary condition with the DS is also know as the Bohm criterion. Further, the total energy drop across the Chodura and Debye sheaths is limited to $\sim 3kT_e$.

The fluid model by Stangeby [17] expanded on the work of Chodura and established that the DS disappears for magnetic field angles below an incidence angle threshold. The critical angle (α^*) for the disappearance of the DS is given by

$$\alpha^* \equiv \sin^{-1}\left\{\left[\left(\frac{2\pi m_e}{m_i}\right)\left(1+\frac{T_i}{T_e}\right)\right]^{1/2}\right\} \qquad (1)$$

where T_e is the electron temperature, T_i the ion temperature, m_i is the mass of the main ion species and m_e is the electron mass. Note that α is the angle the magnetic field makes with the surface. In the CTH experiment the incidence angle is $\alpha \sim 10°$ and the DS does not disappear as it is larger than the crital angle $\alpha^* \approx 4.7°$. For extrapolation to DIII-D or ITER, the DS will disappear leaving only the CS.

The sheath model utilized in this work is that of Stangeby's [17] taking the form of a Python code with the following parameters: electron temperature, ion temperature, bulk density, mass of the main ion species, magnetic field strength and angle that the magnetic field makes with a surface. An electron density profile through the sheath is computed for CR

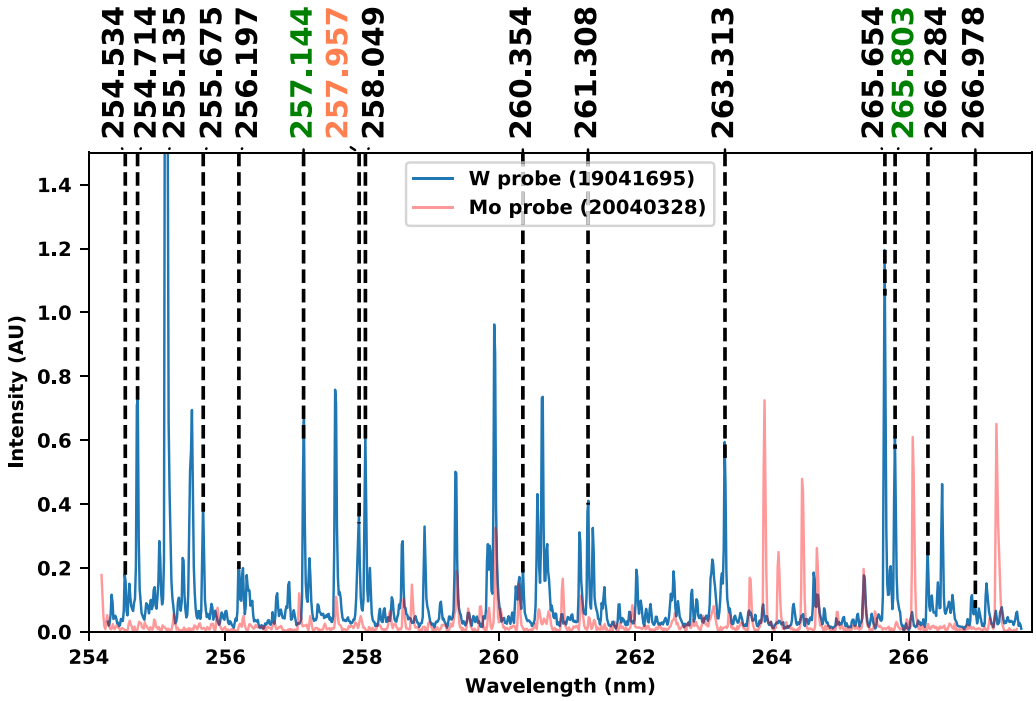

Figure 2. Observed spectra in the CTH experiment with a tungsten tipped probe (blue) and a molybdenum tipped probe (transparent red). W I spectral lines (black), W II spectral lines (green) and W III spectral lines (orange) are all identified by the NIST observed wavelengths and the dashed lines.

modeling. The electron temperature is assumed to be constant across the sheath region; however, particle simulations suggest there is temperature variation within the sheath [18]. The complexity of temperature variations has not been included in this model. Variations within the sheath could create similar effects to the addition of a density gradient; although, a new study would have to be completed to assess these effects. The focus here is on the electron density effects in the sheath and its effects on the time dependence of the tungsten atomic populations.

2.3. Experimental method

The CTH device is a five-fold symmetric torsatron [19] limited at five locations by C, Mo and stainless steel. Tungsten can be introduced into the CTH experiment with a vertically translating W-tipped probe similar to the probe described by Johnson *et al* [20]. Unique to this experiment was the addition of a swept single-tipped Langmuir Probe (LP) embedded into the larger tungsten tipped probe allowing for electron temperature and density measurements (T_e & n_e) which are free parameters used in CR modeling. The design utilized boron nitride (BN) to insulate the LP tip from the tungsten slug. Thus, the probe tip is separated from the tungsten block by approximately 100 Debye lengths, so the LP tip should sample the bulk plasma. The probe was swept between -200 and $\sim$5 V using a triangle waveform at 443 Hz.

A Princeton Instruments IsoPlane SCT 320 Schmidt-Czerny-Turner spectrometer [21] was used in combination with a Andor Newton DU920P-BU2 CCD to obtain tungsten spectroscopy measurements. Spectral data presented in this paper utilized a 4320 grooves/mm grating producing a dispersion of 0.506 nm mm^{-1} on the CCD (0.013 nm/pixel). Both the grating of the spectrometer and CCD were optimized for UV wavelengths where low charge states of tungsten emit most intensely [12]. Tungsten emission light levels allowed a 500 Hz frame-rate producing multiple spectra for each $\sim$100 ms CTH discharge. Example spectra from CTH for both tungsten (blue) and molybdenum (red) tipped probes inserted past the last closed flux surface is shown in figure 2 with spectral lines associated with low charge states identified by the values of Kramida and Shirai [22]. There is relatively little contamination from background impurity species, however spectral lines could be blended with other emission lines from neutral tungsten or higher charge states. The use of two probe tips of different materials allowed for tungsten emission lines to be positively identified.

3. Time dependent tungsten emission and ionization within the sheath

Neutral tungsten emission is modeled using a CS model for the magnetic sheath that also includes a DS when present ($\alpha > \alpha^*$). Tungsten impurity atoms are assumed to sputter from a surface with a ballistic velocity (neutral particles are not affected by magnetic fields). The neutral tungsten velocity is taken to be half the binding energy of neutral tungsten (4.32 eV $\sim$ 2200 m s^{-1}). While in reality there is a distribution in sputtering angle, the model here assumes that all tungsten is sputtered normal to the surface.

In order to obtain a quantitative value of the S/XB parameter, it is crucial to consider the distribution of angle and speed, which varies depending on the specific application. Notably, the distribution would differ between a linear plasma with a biased target and a tokamak. The parameters' distributions have been extensively studied by Eckstein [23] and are also addressed in surface models like F-TRIDYN or RUSTBCA. When applying these distributions directly to experimental scenarios, a trace impurity transport code such as GITR or ERO that include a sheath model would be required for accurate quantitative values. For the purpose of this study, we have selected values that offer a simplified model, yet remain a good approximation over a wide range of experimental conditions.

The velocity of the tungsten sputtered from the surface is used to determine the time that the tungsten exists within the sheath. ColRadPy is then used to time-dependently solve the CR system of equations.

The assumption that tungsten atoms are only sputtered normal to the surface results in tungsten spending a minimum amount of time within the sheath region. Therefore, effects due to the sheath are a lower bound on the actual modifications of the collisional radiative coefficients. Additionally, tungsten that is sputtered from the surface is assumed to start in the ground state; there is experimental evidence of this in neutral molybdenum [24]. However, starting in the ground state is a significant assumption of the model and will be addressed later in section 3.1.

For fusion relevant plasma conditions, neutral tungsten is generally ionized within the magnetic sheath. Even at moderate electron densities (modeled for CTH figure 3(*a*) $T_e = 20\,\text{eV}$, $n_e = 5 \times 10^{12}\,\text{cm}^{-3}$) and electron temperatures greater than 5 eV, neutral tungsten is fully ionized within the magnetic sheath. The ionization rate will change through the density profile of the sheath; however, the total ionization rate (SCD) at the bulk temperature and density (at the sheath entrance) is $\sim 5.5 \times 10^{-8}$ ions s^{-1} cm^3 and is the reason that neutral tungsten ionizes so quickly in the sheath. The total population of neutral tungsten (the blue line) through the sheath region is shown in figure 3(*b*) with total singly ionized tungsten population in orange. The neutral tungsten is completely ionized within the sheath. In situations where not all of the W^0 has ionized within the sheath, the model beyond the sheath uses the bulk plasma density until at least 99% of the W^0 has been ionized. Figure 3(*b*) also shows the ground state population of neutral tungsten in the sheath as the green line. The faster decay of ground state population compared with total neutral tungsten population is a result of significant population being stored in other metastable states of neutral tungsten. The electron temperature is assumed to be constant (at the bulk plasma value) in the sheath region for this model; however, Particle in Cell (PIC) simulations would suggest there is a moderate temperature change, but that is not considered here [25]. Additionally, PIC simulations would also suggest that the electron distribution is non-Maxwellian, however, temperature distributions in this work are assumed to be Maxwellian [26].

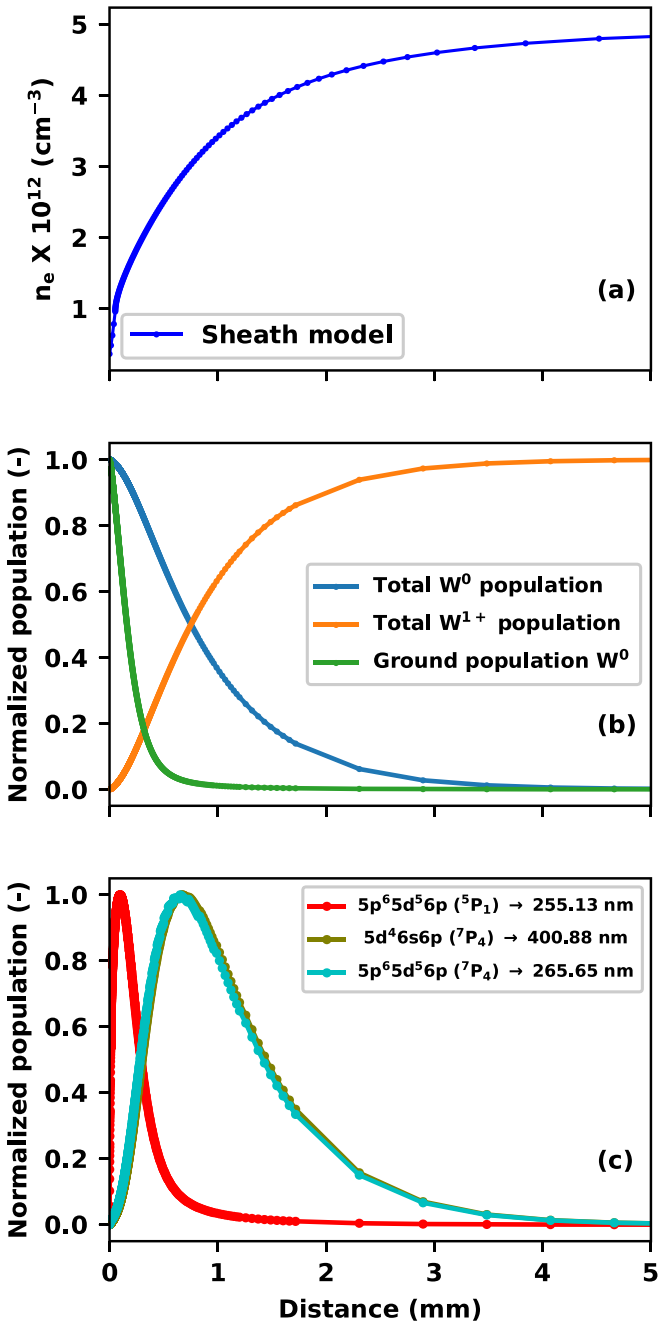

Figure 3. The electron density profile in the Debye (∼0.1 mm) and CSs (∼7 mm) for typical CTH parameters (*a*), W^0 and W^{1+} population with distance from the wall assuming a tungsten speed of 2128 m s^{-1} (half of the tungsten binding energy) (*b*) . The normalized population of levels that produce intense spectral lines (*c*).

The different time dynamics of the excited states that are populated from the $^5D_0$ ground state and the $^7S_3$ metastable state are evident in figure 3(*c*). Level $5p^65d^56p$ ($^5P_1$) which produces the 255.13 nm spectral line is mainly populated from the ground state while the other two levels $5d^46s6p$ ($^7P_4$) and $5p^65d^56p$ ($^7P_4$) which produce the 400.88 and 265.65 nm

emission lines are populated mainly from the $^7S_3$ metastable state [12]. Thus the 265.65 nm line is expected to behave in a similar way to the widely used 400.87 nm line and can be used in comparison with the more pure ground-populated 255.13 nm line. As a result of being populated directly from the ground state, the population in the $5p^6 5d^5 6p$ ($^5P_1$) level is largest close to the surface. All tungsten atoms in the model begin in the ground state, therefore, time is needed for population to transfer to the $^7S_3$ metastable state which populates the excited states which produce the 265.65 and 400.88 nm spectral lines and peak farther into the sheath than the 255.13 nm emission line. While having different upper levels, the 265.65 and 400.88 nm lines behave similarly because they are both dominantly populated from the $^7S_3$ metastable state. Note that lines produced by excited states populated from the metastable levels will emit in a higher electron density region compared with lines populated mainly from the ground state.

The sheath model can modify calculated GCR coefficients at high electron densities. Previous efforts to model the 400.9 nm neutral tungsten S/XB within the CS assumed that tungsten populations were in equilibrium concentrations throughout the sheath [27]. The model presented here differs by including time-dependent effects that can arise from the low density environment of the sheath. The modification to the S/XB coefficient for various spectral lines are included in figure 4. The steady-state bulk model assumes the density from the bulk plasma for collisional radiative modeling. Note that steady-state S/XB values have been utilized in most tungsten spectroscopic erosion measurements where no sheath was considered; this could induce errors as neutral tungsten emits mostly within the sheath. The steady-state sheath model including only the effects of the density gradient within the sheath is equivalent to the work by Guterl *et al* [27]. The fully time-dependent solution includes both the effects of density as well as time-dependent effects assuming the model discussed in section 3. The S/XBs are modified most significantly for high electron densities because more emission comes from the volume closer to the surface (farther from bulk density and therefore farther from the equilibrium conditions of the bulk T_e and n_e). The concentrated emission near the emitting surface for high electron densities is a result of the total effective ionization rate (ionization increases significantly with density). At lower electron densities, tungsten is able to travel farther through the sheath before being ionized, so it will emit closer to the bulk density.

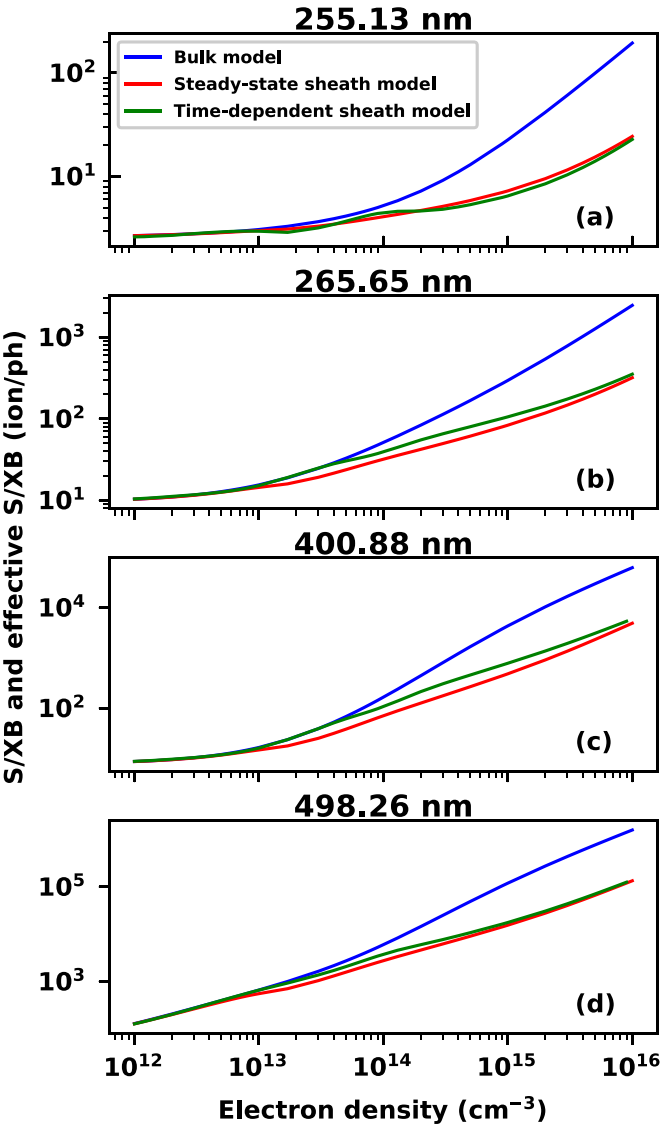

Figure 4. Comparison of neutral tungsten S/XB coefficients as a function of electron density for $T_e = 20$ eV for three different sheath models: bulk S/XB (blue), steady-state sheath effective S/XB (red) and time dependent sheath effective S/XB (green).

3.1. Impact of the initial metastable fraction

The initial ground and metastable fraction is important for tungsten CR modeling using the time-dependent sheath model. As stated in section 3, tungsten is assumed to sputter from a PFC in the ground state. The initial state of tungsten when assumed to sputter into the ground state, is far from the equilibrium metastable fraction for a given T_e and n_e pair. The time for tungsten population to reach equilibrium is linearly dependent on electron density [12]. For reference, tungsten sputtered into a 29 eV plasma at 1×10^{13} cm^{-3} density will take $\sim 2 \times 10^{-5}$ s to reach equilibrium.

The initial state is far from the equilibrium metastable fraction for a given T_e and n_e pair. Figure 5 highlights the equilibrium fractional population in the $^7S_3$ metastable state versus electron density at multiple temperatures. Note that the $^7S_3$ metastable can account for up to 7% of the total population, which is much greater than fractional populations of metastable states in low-Z species [14]. The decrease in the population of the $^7S_3$ level with electron density can be understood similar to light systems where populations in metastable levels decrease with increasing electron density due to electron collisions. The $^7S_3$ also decreases in population with temperature because transferring population from the $^5D_0$ ground state requires a spin changing transition. Rate coefficients for spin changing transitions decrease rapidly with increased electron temperature; therefore, the relative metastable population is inversely proportional to electron temperature.

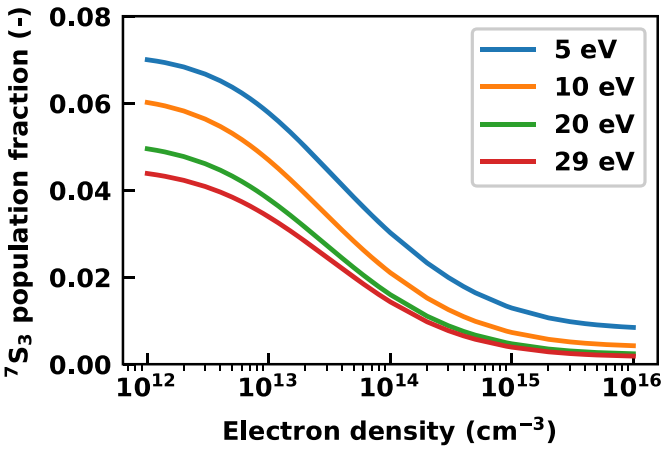

Figure 5. Steady-state population fractions of the $^7S_3$ energy level in neutral tungsten versus electron density for multiple electron temperatures.

It is quite possible the assumption that tungsten is sputtered into the ground state is incorrect. Figure 6 investigates the impact of various initial fractions of tungsten sputtered into the $^7S_3$ metastable state on the effective S/XBs for the W I 400.88 nm and W I 255.13 nm lines. The 400.88 nm line is mainly dependent on the $^7S_3$ metastable, and the 255.13 nm line is mainly dependent on the $^5D_0$ ground state. As a result, these two S/XB coefficients should be sensitive to the relative population in each driving state. The impact of the initial metastable fractional on the S/XB is clear for the 400.88 nm spectral line. The S/XB decreases with increasing initial $^7S_3$ population because the 400.88 nm line is populated faster within sheath as population does not need to first transfer from $^5D_0$ (ground state) the $^7S_3$ (metastable state) to then populate the $5p^6 5d^5 6p$ ($^7P_4$) level producing the 400.88 nm line.

3.2. *Impact of sputtering velocity*

Another assumption of the model discussed in section 3 is that the sputtered velocity is equal to half the binding energy of the neutral tungsten ($\sim$2128 m s^{-1}). In reality, there will be a distribution of sputtered velocities and additionally a distribution of sputtered angles making the average velocity of sputtered tungsten normal to the PFC surface likely less than 2128 m s^{-1}. The variation of the W I S/XBs for the 400.88 nm and 255.13 nm lines due to changes in the sputtering velocity is shown in figures 7(*a*) and (*b*). The steady-state S/XB (non-sheath model) for the 400.88 nm line in figure 7(*a*) is plotted alongside the time-dependent effective S/XB (CS model) for slower and faster sputtering velocities. While there is an interplay of CR effects that impact the dependence of the S/XB on density, the S/XB coefficient corresponding to a 10 times increase in velocity is larger because the tungsten atoms spend less time in the low density region of the sheath. Conversely, tungsten sputtered at slower velocities spend more time in the less dense region and the S/XB decreases. The simple

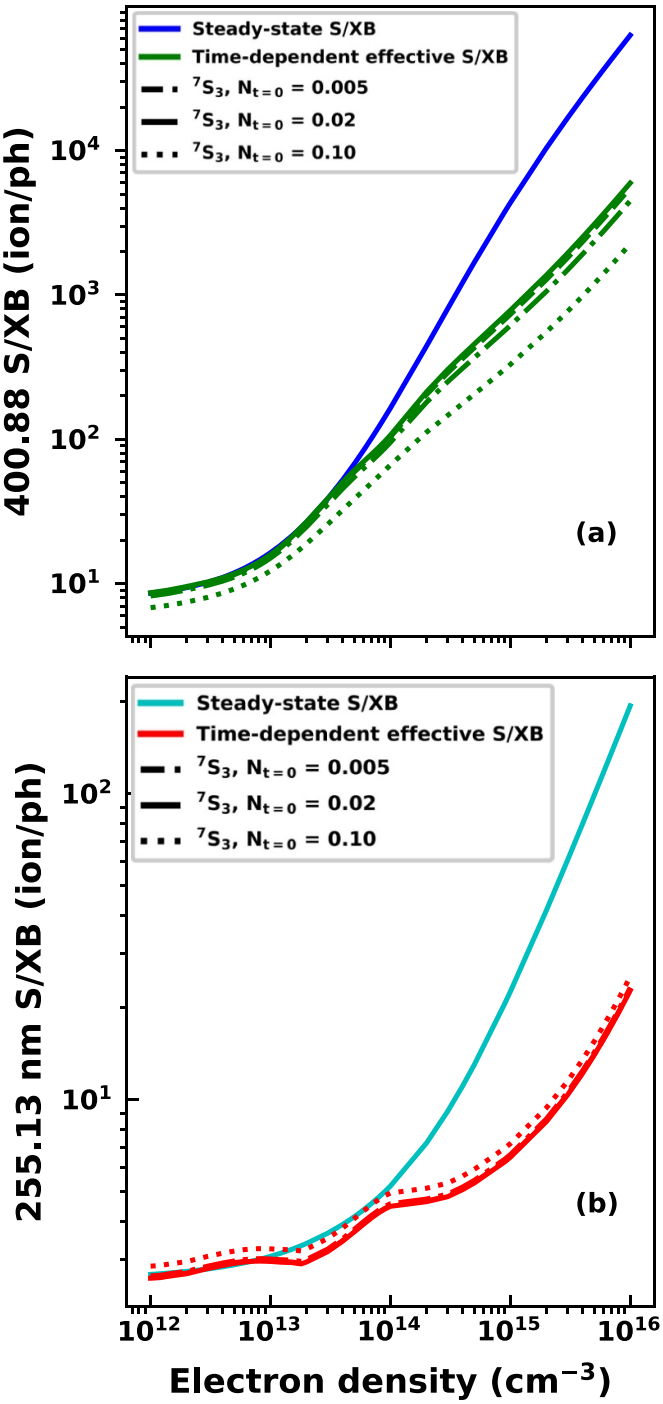

Figure 6. Comparison of W I 400.88 nm (*a*) and 255.13 nm (*b*) S/XBs versus n_e, at $T_e = 20$ (eV) for various initial metastable fractions. The steady-state S/XBs are in blue (400.9 nm) and cyan (255.13 nm), while the time-dependent CS model is in green (400.9 nm) and red (255.13 nm). Variations of the sputtering velocity are indicated by the dashed and dash-dot lines.

picture of the 255.13 nm S/XB is that at higher electron density (faster velocity) ionization increases giving rise to a larger S/XB. At low electron densities, the SCD (total ionization rate) decreases, so for lower velocities tungsten atoms spend more time in the low density sheath region and the S/XB decreases.

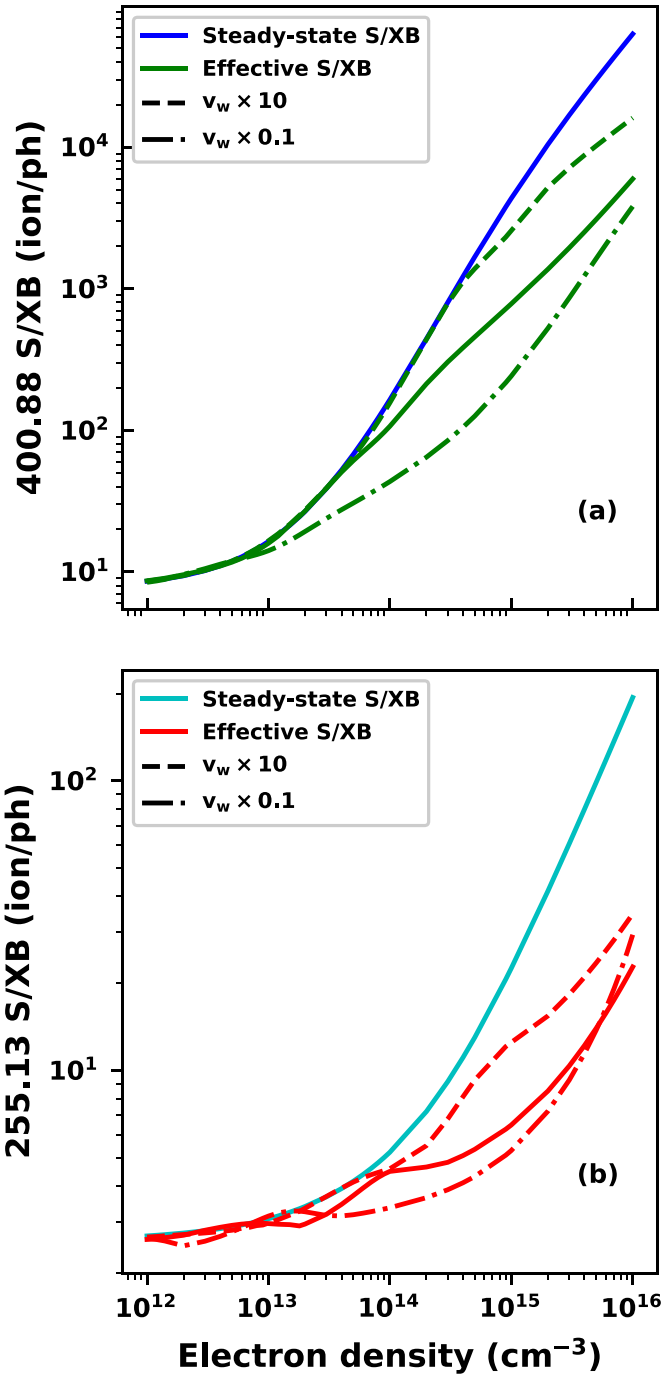

Figure 7. Comparison of W I 400.88 nm (*a*) and 255.13 nm (*b*) S/XBs versus n_e, at $T_e = 20$ (eV) for various sputtering velocities (plotted as the dashed lines). The steady-state S/XBs are in blue (400.9 nm) and cyan (255.13 nm), the time-dependent CS model is shown in green (400.9 nm) and red (255.13 nm). Variations of the sputtering velocity are indicated as the dash-dot and the dashed lines.

The S/XB is also dependent on the PEC, which emits in different parts of the sheath depending on sheath parameters, T_e and n_e and results in the oscillatory behavior of the S/XB.

The variation of the W I 400.88 nm S/XB due sputtering velocity (figure 7(*b*)) is broadly similar to that of the 255.13 nm (figure 7(*a*)); the S/XBs are approximately proportional to the velocity but a bit clearer. At high velocities, more time is spent at higher densities yielding more ionization. The increase in velocity leads to the time-dependent effective S/XB reproducing the bulk S/XB for higher electron densities. The behavior of the 400.88 nm effective S/XB is consistent with the limiting case of large sputtered velocity where the tungsten spends no time within the sheath region and all of its neutral charge state life time in bulk plasma. At lower velocities, tungsten atoms spend more time in the low density region of the sheath, leading to less ionization and a decrease in the S/XB coefficient. Again, the 400.88 nm effective S/XB is consistent with a slow velocity limiting case where the tungsten spends all its time in the low density sheath region, emitting many photons before being ionized.

4. Comparison of electron temperature inferred from CR modeling and LP measurements

The translating probe described in section 2.3 was designed to obtain simultaneous spectroscopic measurements of emission from low charge states of tungsten along with local T_e and n_e from the LP tip. For collisional radiative modeling without a sheath, electron temperature and density are the only two free parameters. When a time-dependent sheath model is considered, other free parameters are introduced; however, T_e and n_e are still the most sensitive parameters for determining collisional radiative coefficients. Therefore, constraining T_e and n_e is required to validate the model against CTH experimental measurements. The spectrometer used for this analysis is described in section 2.3. For all of the data analyzed here, the spectroscopic measurements were acquired at a 500 Hz frame rate, and the LP power supply was swept at 443 Hz. In order to sample different plasma conditions, the tungsten slug with an embedded LP was inserted into the plasma between 28 and 22 cm from the mid-plane the plasma is limited at 26 cm.

4.1. Impact of the sheath on emissivity ratios

In addition to modifying the calculated S/XB coefficients at high electron densities, the addition of a sheath also modifies the emissivity of spectral lines. The emissivity ratio predicted by the bulk model is compared to the time-dependent sheath model in figure 8 for the 255.13 and 265.65 nm lines. Emissivity is compared instead of PECs because emission from spectral lines occurs at different locations within the sheath (see figure 3) and therefore at different electron densities.

The inclusion of the sheath model has a similar impact on the ratio of the calculated emissivities (figure 8) as on the S/XB coefficients (figure 4). As the electron density changes, the emissivity ratio only significantly modified at high electron densities. The sheath model does not alter the emissivity line ratio significantly at densities and temperatures relevant for CTH ($n_e \sim 1 \times 10^{12}\,cm^3$, $T_e \sim 20$ eV); therefore it has not been included in the modeling of CTH plasmas presented in the next section.

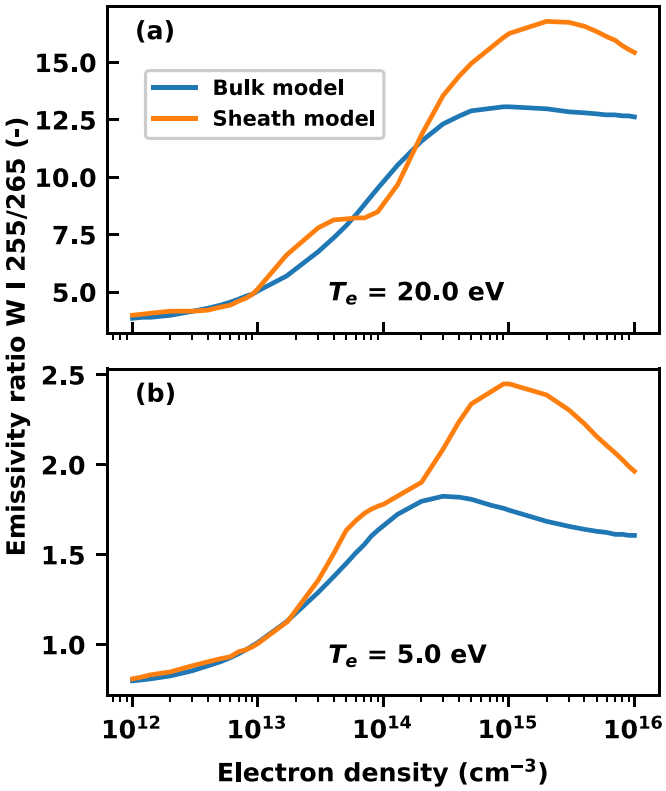

Figure 8. Calculated emissivity ratios for W I 255.13 nm and 265.65 nm spectral lines. The bulk model is plotted in orange and the sheath model is plotted in blue for $T_e = 20$ eV (*a*) and $T_e = 5$ eV (*b*).

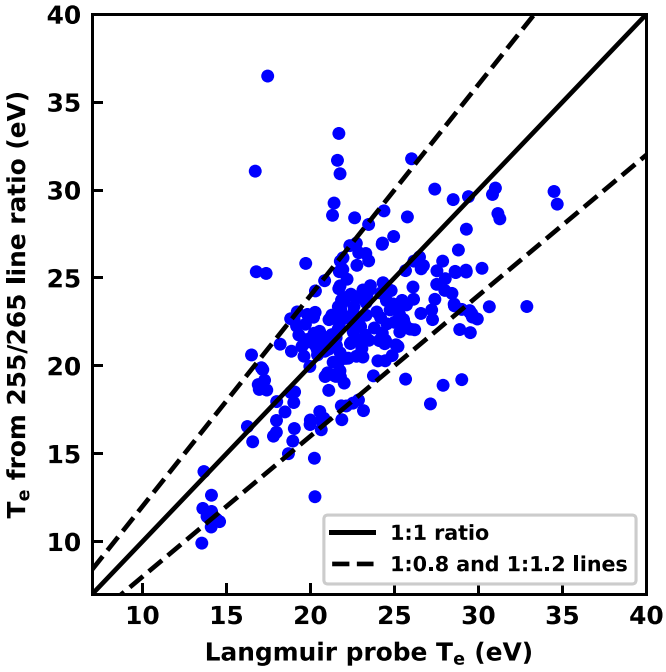

Figure 9. Comparison of electron temperatures measured by the embedded LP and inferred from collisional radiative modeling using spectroscopy observations of the 255.13 nm and 265.65 nm W I lines.

4.2. Validating time-dependent CR modeling against CTH experimental measurements

The analysis of spectroscopic and Langmuir probe measurements to determine electron temperature included the following assumptions. Electron temperature and density were assumed to be constant during each spectroscopy exposure (2 ms). While no relative intensity calibration was available for the two W I lines at 255.13 nm and 265.65 nm, the two spectral lines are close enough in wavelength that differences in the relative intensities should be small. Collisional radiative modeling to determine the electron temperature utilized the density measured by the LP. It can be seen that the emissivity ratios for CTH relevant densities (figure 8) are not sensitive to electron density (a good line ratio for temperature diagnosis is strongly dependent on electron temperature and weakly dependent on electron density.)

The inferred electron temperature from CR modeling of the 255.13–265.65 nm line ratio and the temperature measured by the LP are compared to a 1:1 line in figure 9. The data set includes multiple probe depths allowing for a variation of electron temperature and density. Measurements were selected during the middle of the CTH discharge excluding the current ramps yielding relatively steady-state plasmas. Tungsten emission is very localized to the probe, neutral tungsten at CTH densities is almost entirely ionized within 2 mm of the LP surface as seen in figure 3. The optical line of sight was aligned to the tungsten probe as was done Johnson *et al* [20]. The relatively good agreement between the LP and the line ratio technique provides an initial validation of the atomic data [13] and sheath model. To fully verify the atomic data and time-dependent model, additional experiments at higher electron densities are needed to observe modifications due to time-dependent sheath effects. The model could be farther expanded to include error propagation from atomic rates as well as non-Maxwellian rates.

5. Conclusions

A consequence of shallow magnetic angles relative to PFCs is the formation of a large MPS that produces a relatively large region of low density near plasma facing components. Low density environments can lead to tungsten atoms spending significant time away from equilibrium conditions making time-dependent metastable effects important. New time-dependent collisional radiative modeling was developed to model tungsten emission as it is eroded and transports through the low density MPS. S/XB coefficients for neutral tungsten emission lines are potentially modified up to a factor of 10 for ITER relevant divertor electron temperatures and densities. The S/XB coefficient for the W I 255.13 nm spectral line (dominated by the ground state) showed a very different behavior from the 400.88 nm W I emission line (dominated by the $^7S_3$ metastable state). Suggesting

the use of multiple spectral lines associated with different metastable levels would be beneficial for gross erosion diagnosis.

The wavelength range from 254 to 267 nm has been identified to observe emission from low charge states of tungsten as there is a high density of neutral tungsten lines with different metastable level dependencies allowing for time-dependent effects arising from MPSs to be measured. A relatively high resolution spectrometer is capable of simultaneously observing the entire 254–267 nm wavelength range. Additionally, there are spectral lines from W^{+} and W^{2+} present in this wavelength range, which can be utilized for prompt re-deposition investigations.

Time-dependent models demonstrate there is a significant loss of population from the ground state to other metastable states with the loss rates to metastable states often larger than the ionization rates in contrast with low-Z species where metastable states only contain a small population relative to the ground state. The large number of metastable levels with significant population requires time-dependent metastable effects to be considered for modeling of ITER relevant electron densities.

The comparison of temperature measurements from a LP and spectroscopic line ratios exhibits good agreement for CTH plasma conditions providing confidence in the validity of the calculated rates [13]. Further work is needed for a variety of electron temperature and densities but high-density regimes would be of particular interest as time-dependent metastable states are predicted to become increasingly important under those conditions.

Acknowledgments

Work supported by U.S. Department of Energy Grants DE-SC0015877 and DE-FG02-00ER54610. This research was also supported by the U.S. Department of Energy Fusion Energy Sciences Postdoctoral Research Program administered by the Oak Ridge Institute for Science and Education (ORISE) for the DOE. ORISE is managed by Oak Ridge Associated Universities (ORAU) under DOE Contract Number DE-SC0014664. All opinions expressed in this paper are the author's and do not necessarily reflect the policies and views of DOE, ORAU, or ORISE.

ORCID iDs

C.A. Johnson https://orcid.org/0000-0002-5640-5854
D.A. Ennis https://orcid.org/0000-0002-4833-5884
S.D. Loch https://orcid.org/0000-0002-3822-6756
C.P. Ballance https://orcid.org/0000-0003-1693-1793

References

[1] Stangeby P.C. 2011 Assessing material migration through ^{13}C injection experiments *J. Nucl. Mater.* **415** S278–83
[2] Pütterich T., Neu R., Dux R., Whiteford A.D., O'Mullane M.G. and Summers H.P. (the ASDEX Upgrade Team) 2010 Calculation and experimental test of the cooling factor of tungsten *Nucl. Fusion* **50** 25012
[3] Holtrop K., Buchenauer D., Chrobak C., Murphy C., Nygren R., Unterberg E. and Zach M. 2017 The design and use of tungsten coated TZM molybdenum tile inserts in the DIII-D tokamak divertor *Fusion Sci. Technol.* **72** 634–9
[4] Abrams T. *et al* Design and physics basis for the upcoming DIII-D SAS-VW campaign to quantify tungsten leakage and transport in a new slot divertor geometry *Phys. Scr.* **96** 124073
[5] Donovan D.C. *et al* 2018 Utilization of outer-midplane collector probes with isotopically enriched tungsten tracer particles for impurity transport studies in the scrape-off layer of DIII-D (invited) *Rev. Sci. Instrum.* **89** 115
[6] Geier A., Asmussen K., Bard A., Neu R. and Krieger K. 1999 A sublimation probe for the injection of high-Z impurities into fusion devices *Rev. Sci. Instrum.* **70** 63
[7] Eksaeva A., Marenkov E., Borodin D., Kreter A., Reinhart M., Kirschner A., Romazanov J., Terra A., Brezinsek S. and Nordlund K. 2017 ERO modelling of tungsten erosion in the linear plasma device PSI-2 *Nucl. Mater. Energy* **12** 253–60
[8] Abrams T. *et al* 2017 The inter-ELM tungsten erosion profile in DIII-D H-mode discharges and benchmarking with ERO+OEDGE modeling *Nucl. Fusion* **57** 056034
[9] Brezinsek S., Borodin D., Coenen J., Kondratjew D., Laengner M., Pospieszczyk A. and Samm U. 2011 Quantification of tungsten sputtering at W/C twin limiters in TEXTOR with the aid of local WF 6 injection *Phys. Scr.* **2011** 014016
[10] Van Rooij G.J. *et al* 2013 Tungsten divertor erosion in all metal devices: Lessons from the ITER like wall of JET *J. Nucl. Mater.* **438** S42–S47
[11] Behringer K., Summers H.P., Denne B., Forrest M. and Stamp M. 2000 Spectroscopic determination of impurity influx from localized surfaces *Plasma Phys. Control. Fusion* **31** 2059–99
[12] Johnson C.A., Loch S.D. and Ennis D.A. 2020 The effect of metastable atomic levels in neutral tungsten for erosion and impurity transport applications *Plasma Phys. Control. Fusion* **62** 125017
[13] Smyth R.T., Ballance C.P., Ramsbottom C.A., Johnson C.A., Ennis D.A. and Loch S.D. 2018 Dirac R -matrix calculations for the electron-impact excitation of neutral tungsten providing noninvasive diagnostics for magnetic confinement fusion *Phys. Rev.* A **97** 052705
[14] Summers H.P., Dickson W.J., O'Mullane M.G., Badnell N.R., Whiteford A.D., Brooks D.H., Lang J., Loch S.D. and Griffin D.C. 2006 Ionization state, excited populations and emission of impurities in dynamic finite density plasmas: I. The generalized collisional radiative model for light elements *Plasma Phys. Control. Fusion* **48** 263–93
[15] Johnson C.A., Loch S.D. and Ennis D.A. 2018 ColRadPy : a python collisional radiative solver *Nucl. Mater. Energy* **20** 100579
[16] Chodura R. 1982 Plasma-wall transition in an oblique magnetic field *Phys. Fluids* **25** 1628–33
[17] Stangeby P.C. 2012 The Chodura sheath for angles of a few degrees between the magnetic field and the surface of divertor targets and limiters *Nucl. Fusion* **52** 083012
[18] Wesson J.A. 1995 Effect of temperature gradient on plasma sheath *Plasma Phys. Control. Fusion* **37** 1459–66
[19] Hartwell G.J., Knowlton S.F., Hanson J.D., Ennis D.A. and Maurer D.A. 2017 Design, construction and operation of the Compact Toroidal Hybrid *Fusion Sci. Technol.* **72** 76–90

[20] Johnson C.A. *et al* 2019 Advances in neutral tungsten ultraviolet spectroscopy for the potential benefit to gross erosion diagnosis *Plasma Phys. Control. Fusion* **61** 095006
[21] Princeton Instruments 2013 IsoPlane manual version 1.B (available at: www.princetoninstruments.com/wp-content/uploads/2020/04/IsoPlane-SCT-320-Manual-Issue-2-4411-0143-1.pdf)
[22] Kramida A.E. and Shirai T. 2006 Compilation of wavelengths, energy levels and transition probabilities for W I and W II *J. Phys. Chem. Ref. Data* **35** 423–683
[23] Eckstein W. 2002 Calculated sputtering, reflection and range values *IPP Report 9/132* Max Planck Institute for Plasma Physics
[24] Marenkov E., Gutorov K. and Sorokin I. 2018 Radiation of high-Z atoms sputtered by plasma *Nucl. Instrum. Methods Phys. Res.* B **436** 257–62
[25] Tskhakaya D. 2016 Kinetic modelling of the plasma recombination: kinetic modelling of the plasma recombination *Contrib. Plasma Phys.* **56** 698–704
[26] Tskhakaya D. 2017 One-dimensional plasma sheath model in front of the divertor plates *Plasma Phys. Control. Fusion* **59** 114001
[27] Guterl J., Johnson C., Ennis D., Loche S. and Snyder P. 2019 Effects of the Chodura sheath on tungsten ionization and emission in tokamak divertors *Contrib. Plasma Phys.* 1–7